CHAPTER 4

THERMOELASTIC DAMPING AND VIBRATION ANALYSIS FOR MICRO-BEAM RESONATORS BASED ON MOORE-GIBSON THOMPSON HEAT CONDUCTION MODEL

4.1 Thermoelastic Damping Analysis for Micro-Beam Rasonators in the Frame of Moore-Gibson-Thompson (MGT) Thermoelasticity Theory considering Size Effects

4.1.1 Introduction[1]

Rapid advancements of the micro and nanotechnologies have generated various micro and nano scale structures, as for example Micro and nano resonators, which are of interest to both the scientific community and engineering fields. Resonator is a device or system that exhibits resonance or resonant behavior. It naturally oscillates with greater amplitude at some frequencies, called resonant frequencies, than at other frequencies. Due to their small sizes and low weight, micro and nanomechanical resonators can oscillate at very high resonant frequencies, which provides them with a remarkable

[1]The content of this sub chapter is published in Waves in Random and Complex Media, 1-18, 2021.

ability to perform both sensing and detecting in advanced technological applications, including ultra sensitive mass and force sensing, ultra low-power radio frequency (RF) signal generation and timing, chemical and biological sensing, cooling, environmental control, and quantum measurement. In order to design high-performance mechanical resonators, the understanding of damping effects is important. Damping in Micromechanical resonators represents the all of the processes by which the energy associated with the vibration of the resonator decays over time. Thermoelastic damping (TED) is one of the most important loss mechanisms for micro and nanobeam resonators among all the loss mechanisms. TED is totally based on the thermal and elastic nature of the body. Many investigations have shown the experimental evidences about TED in intrinsic losses for the flexural micro and nanobeam resonators. It is impossible to remove TED completely, however, it can only be reduced by design or fabrication of suitable resonators. TED is observed to be the keystone that affects the performance of he vacuum-operated micro and nanobeam resonators and the estimation of thermoelastic damping (TED) in micro and nano-mechanical resonators is a significant aspect of acquiring a high quality factor (QF). The quality factor measures the resonance behavior or performance of resonators. A high value of QF implies better identification of less damping and better sensitivity.

This chapter deals with the TED analysis for two different beams, namely Euler–Bernoulli beam model and Timoshenko beam in the context of MCST. It has two subchapters. The present subchapter 4.1 adopts the frequency approach method to derive the size-dependent expression of the inverse quality factor for evaluating TED in rectangular micro/nano-beam resonator. In the context of the complex frequency method, the expression of the inverse quality factor is $Q^{-1} = 2|\mathrm{Im}(\omega)/\mathrm{Re}(\omega)|$, where the real part (Re) and the complex part (Im) of the frequency ω provide new eigen frequencies and attenuation of vibration, respectively.

Eminent researchers have presented some pioneering work in the field of TED anal-

ysis. The TED behavior (energy dissipation mechanism) in the flexural resonator for the simple beam was first studied by Zener (1937; 1938). Thereafter, the modification of Zener's work was done by Lifshitz and Roukes (2000). They analyzed that the energy dissipation of micro resonators increases significantly with the decrease of size of the beam. Hosseini (2018) obtained the analytical solution for heat- affected MEMS/NEMS beam resonator for non-locally coupled thermoelasticity based on Green-Naghdi theory (1993). The size-dependent TED analysis for electrically actuated micro-beams and utilizing the couple stress theory in the context of DPL thermoelasticity is studied by Borjalilou et al. (2019). Later on, Kumar and Mukhopadhyay (2020) investigated the TED analysis for size-dependent microplate resonators utilizing the modified couple stress theory in the context of the TPL heat conduction model presented by Roychoudhuri (2007).

Being inspired from above effective findings, the present subchapter of the thesis attempts to investigate TED in micro/nano-beam resonators utilizing modified couple stress theory (MCST) under the Moore-Gibson-Thompson (MGT) generalized thermoelasticity theory (Quintanilla (2019)). Subsection 4.1.2 gives brief details of the modified couple stress theory (MCST) and derives a coupled heat conduction equation based on the MGT thermoelasticity theory. For small flexural vibration, the TED in the rectangular cross-section of a thin beam is analyzed by using the complex frequency method based on MCST in Subsection 4.1.3. An explicit analytical expression for QF has been derived for the microbeam resonator in Subsection 4.1.4. Furthermore, the impact of the material length scale parameter on TED associated with MCST for silicon micro-beam resonator is investigated in detail by comparing the present results with those predicted by classical continuum theory (CCT). The obtained results are also compared with the existing results for the Lord-Shulman (LS) and Green-Naghdi (GN-III) thermoelasticity theories. Lastly, some importance conclusions regarding TED in micro-beam resonators in the present context are highlighted.

4.1.2 Problem formulation

4.1.2.1 Basics of the modified couple stress theory (MCST)

Yang et al. (2002) introduced the modified couple stress theory (MCST) theory for very small deformations of a continuous spectrum in an isotropic material by considering the strain energy density U_s as a function of both the strain tensor and the curvature tensor occupying a volume V in space. This modified theory makes it easier to appropriately model the structures at micro and nano scale. The defined tensors in MCST satisfy

$$U_s = \iiint_V \left(\sigma_{ij} e_{ij} + \Upsilon_{ij}\chi_{ij}\right) dV, \tag{4.1.1}$$

$$\chi_{ij} = \frac{1}{2}\left(\frac{\partial v_i}{\partial x_j} + \frac{\partial v_j}{\partial x_i}\right), \tag{4.1.2}$$

$$v_i = \frac{1}{2}\left(\mathrm{curl}(\boldsymbol{u})\right)_i, \tag{4.1.3}$$

where v_i represents the components of the infinitesimal rotation vector $\boldsymbol{v}$. σ_{ij} and Υ_{ij} are the elements of the symmetric part of the Cauchy stress tensor $\boldsymbol{\sigma}$ and the deviatoric part of the couple stress tensor $\boldsymbol{\Upsilon}$ for the elastic material, respectively, defined by

$$\sigma_{ij} = \lambda e_{kk}\delta_{ij} + 2\mu e_{ij} - (3\lambda + 2\mu)\,\alpha_t\,\theta\delta_{ij}, \tag{4.1.4}$$

$$\Upsilon_{ij} = 2\mu l^2 \chi_{ij}. \tag{4.1.5}$$

Here, Lame constants can be written as $\lambda = \frac{E\vartheta}{(1+\vartheta)(1-2\vartheta)}$ and $\mu = \frac{E}{2(1+\vartheta)}$. l represents the material length scale parameter and χ_{ij} represents the component of the rotation gradient tensor. For the linear elastic material, the components of the strain tensor in terms of stress components and other parameters are expressed as

$$e_{ij} = \frac{1}{E}\left[(1+\vartheta)\,\sigma_{ij} - \vartheta\sigma_{kk}\delta_{ij}\right] + \alpha_t\theta\delta_{ij}.$$

4.1.2.2 Coupled heat conduction equation based on Moore-Gibson-Thompson (MGT) thermoelasticity

Green and Naghdi proposed three new theories regarding heat conduction which are subsequently called as theroelasticity theory of type I, II, and type III. The fusion of the GN-III theory (1993) and Lord and Shulman thermoelasticity theory (1967) with the linearized MGT heat conduction equation as introduced in the Quintanilla Moore-Gibson-Thompson (MGT) model (2019) for isotropic material is described as follows:

$$\boldsymbol{q} + \tau_q \frac{\partial \boldsymbol{q}}{\partial t} = -\left(K\nabla T + K^*\nabla \upsilon\right), \tag{4.1.6}$$

where υ refers to thermal displacement that satisfies

$$\dot{\upsilon} = T. \tag{4.1.7}$$

For an isotropic solid body, a form of conservation of energy in the absence of heat source is taken by

$$-\nabla \boldsymbol{q} = \rho c_E \frac{\partial T}{\partial t} + \frac{T_0 E \alpha_t}{(1-2\vartheta)} \frac{\partial \boldsymbol{e}}{\partial t}, \tag{4.1.8}$$

The above relationship is a fusion of volumetric strain, temperature, and heat flux for the isotropic thermoelastic body. Therefore, with the help of Eqs. (4.1.6)-(4.1.8), the coupled heat conduction equation in the absence of a heat source is obtained for the Moore-Gibson-Thompson (MGT) thermoelasticity theory as

$$K\nabla^2\dot{\theta} + K^*\nabla^2\theta = \left(1 + \tau_q \frac{\partial}{\partial t}\right)\left(\rho c_E \ddot{\theta} + \frac{T_0 E \alpha_t}{(1-2\vartheta)}\ddot{\boldsymbol{e}}\right), \tag{4.1.9}$$

where $\theta = T - T_0$ represents the change in temperature from the reference temperature T_0.

4.1.3 Modeling of beam resonator

In most cases, the rectangular cross-section of the beam is employed in MEMS resonators. Therefore, the Cartesian coordinate system is applied to the rectangular cross-section of a micro-beam with length $L\,(0 \leqslant x \leqslant L)$, width $b\,(-\frac{b}{2} \leqslant y \leqslant \frac{b}{2})$

and thickness $h\,(-\frac{h}{2} \leqslant z \leqslant \frac{h}{2})$. For the small flexural displacement of the beam, the length of beam is fixed in $\overrightarrow{x}$ direction, the width along $\overrightarrow{y}$ direction and thickness in the direction of $\overrightarrow{z}$ axis. At the initial temperature T_0 (uniform reference temperature), the movement of small thin beam will be strain-free and unstressed. The beam goes through bending vibrations of small amplitude and the deformation is assumed to be consistent with the linear Euler-Bernoulli theory (Park and Gao (2006)). That is, any rectangular cross-section of a beam initially perpendicular to the beam axis remains rectangular and perpendicular to the neutral axis after bending. It is further taken that the beam's neutral axis is the one that runs through the length of the beam and does not suffer any expansion or contraction during bending, which is similar to Euler Bernoulli's beam theory. In Figs. 4.1.1(a,b), the thin micro beam goes through flexural vibration about $\overrightarrow{z}$ axis. The components of the strain tensor in terms of transverse displacement w are therefore given by (see Borjalilou et al. (2019))

$$e_{xx} = -z\frac{\partial^2 w}{\partial x^2}, \tag{4.1.10}$$

$$e_{yy} = e_{zz} = \vartheta z\frac{\partial^2 w}{\partial x^2} + (1+\vartheta)\,\alpha_t\theta. \tag{4.1.11}$$

Using above Eqs. (4.1.10) and (4.1.11), the resultant volumetric strain can be expressed as

$$e_{kk} = e_{xx} + e_{yy} + e_{zz} = (2\vartheta - 1)\,z\frac{\partial^2 w}{\partial x^2} + 2\,(1+\vartheta)\,\alpha_t\theta. \tag{4.1.12}$$

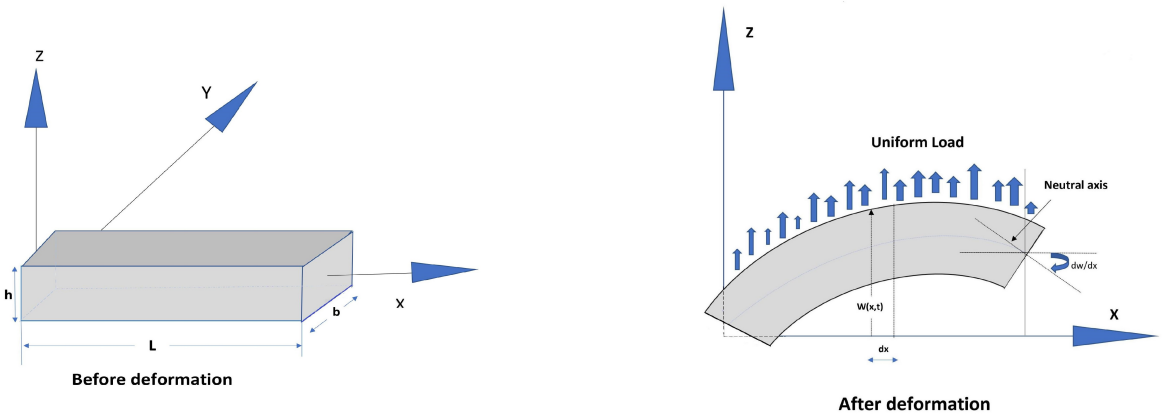

Figure 4.1.1: A schematic of an Euler–Bernoulli beam's deformation.

As per modified couple stress theory for Euler-Bernoulli beam, the equation of motion for thermoelastic coupling is given by (see Park and Gao (2006))

$$\left(EI + \mu Al^2\right) \frac{\partial^4 w}{\partial x^4} + \frac{\partial^2 I_t}{\partial x^2} + \rho A \frac{\partial^2 w}{\partial t^2} = 0. \tag{4.1.13}$$

Together with the above equation, the following boundary conditions are taken at two end sections of the beam $x = 0$ and $x = L$:

$$\left(EI + \mu Al^2\right) \frac{\partial^3 w}{\partial x^3} + \frac{\partial I_t}{\partial x} = 0 \quad \text{or } \delta w = 0, \tag{4.1.14}$$

$$\left(EI + \mu Al^2\right) \frac{\partial^2 w}{\partial x^2} + I_t = 0 \quad \text{or } \delta \left(\frac{\partial w}{\partial x}\right) = 0, \tag{4.1.15}$$

where I is a moment of inertia, I_t denotes the thermal moment of a micro-beam with cross section area $A = bh$, and w is the deflection of the beam.

Therefore, the following is found in the present case:

$$I = \int \int_A z^2 dA = \frac{bh^3}{12}, \tag{4.1.16}$$

and

$$I_t = \int \int_A E\alpha_t \theta z dA = E\alpha_t b \int_{-h/2}^{h/2} \theta z dz. \tag{4.1.17}$$

For thin beams, the temperature changes take place higher along the z-axis (thickness direction), so $\nabla^2\theta$ can be easily replaced by $\frac{\partial^2\theta}{\partial z^2}$. That is, temperature gradient along the y-axis (width direction) is neglected here. Hence, with the help of Eqs. (4.1.10) – (4.1.12), Eq. (4.1.9) yields

$$\left(\frac{K^*}{K} + \frac{\partial}{\partial t}\right) \frac{\partial^2\theta}{\partial z^2} = \frac{1}{\Omega} \left(1 + \tau_q \frac{\partial}{\partial t}\right) \left(\phi \frac{\partial^2\theta}{\partial t^2} - \frac{\triangle_E z}{\alpha_t} \frac{\partial^4 w}{\partial t^2 \partial x^2}\right), \tag{4.1.18}$$

where $\triangle_E = \frac{E\alpha_t^2 T_0}{\rho c_E}$ is the non-dimensional relaxation strength, $\phi = \frac{(1-2\vartheta)+2\triangle_E(1+\vartheta)}{(1-2\vartheta)}$ and $\Omega = \frac{K}{\rho c_E}$ is thermal diffusivity.

4.1.4 Quality factor of TED

For proceeding with TED of the beam resonator, the temperature distribution and transverse displacement functions are assumed as (Lifshitz and Roukes (2000), Park and Gao (2006))

$$w\left(x,t\right)=W_0\left(x\right)\ \exp\ \left(i\omega t\right),\qquad \theta\left(x,y,t\right)=\Theta_0\left(x,y\right)\ \exp\ \left(i\omega t\right), \tag{4.1.19}$$

where ω is the frequency of vibration, W_0 and Θ_0 are both complex valued amplitude functions. Substituting the above expressions (4.1.19) into the Eq. (4.1.18), it is obtained that

$$\frac{\partial^2\Theta_0}{\partial z^2}=\frac{1}{\Omega}\frac{\left(-\omega^2-i\tau_q\omega^3\right)}{\left(\frac{K^*}{K}+i\omega\right)}\left(\phi\Theta_0-\frac{\triangle_E z}{\alpha_t}\frac{\partial^2 W_0}{\partial x^2}\right). \tag{4.1.20}$$

After simplification, Eq. (4.1.20) can be rewritten as

$$\frac{\partial^2\Theta_0}{\partial z^2}+g^2\phi\Theta_0=g^2\frac{\triangle_E z}{\alpha_t}\frac{\partial^2 W_0}{\partial x^2}, \tag{4.1.21}$$

where $g^2=\frac{\omega}{\Omega}\frac{\left(\omega+i\tau_q\omega^2\right)}{\left(\frac{K^*}{K}+i\omega\right)}$.

Also, the complex valued parameter g can be written in the following form:

$$g=\sqrt{\frac{\omega}{\Omega}}\sqrt{\beta_1-i\beta_2}=\frac{\xi\xi_1}{h}-i\frac{\xi}{h\xi_1}\beta_2, \tag{4.1.22}$$

where

$$\xi=h\sqrt{\frac{\omega}{2\Omega}},\quad \xi_1=\sqrt{\sqrt{\beta_1^2+\beta_2^2}+\beta_1},$$
$$\beta_1=\omega\phi\frac{\left[\left(\frac{K^*}{K}+\tau_q\omega^2\right)\right]}{\left[\left(\frac{K^*}{K}\right)^2+\omega^2\right]},\quad \beta_2=\omega\phi\frac{\left[\left(1-\tau_q\frac{K^*}{K}\right)\omega\right]}{\left[\left(\frac{K^*}{K}\right)^2+\omega^2\right]}.$$

The solution to the above Eq. (4.1.21) is given by

$$\Theta_0=\widetilde{A}_1\ \sin\ \left(gz\right)+\widetilde{A}_2\ \cos\ \left(gz\right)+\frac{\triangle_E z}{\alpha_t\phi}\frac{\partial^2 W_0}{\partial x^2}, \tag{4.1.23}$$

where $\widetilde{A}_1$ and $\widetilde{A}_2$ are arbitrary constants.

Next, boundary conditions are considered at both upper and lower surfaces of the beam in the form of adiabatic conditions (which means that there is no heat flow on the top and bottom surfaces of the beam). Therefore, the following is found:

$$\frac{\partial \Theta_0}{\partial z} = 0 \quad \text{at} \quad z = \pm\frac{h}{2}. \tag{4.1.24}$$

In view of the above two Eqs. (4.1.23) and (4.1.24), the values of arbitrary constants $\widetilde{A}_1$ and $\widetilde{A}_2$ are acquired and a complete analytical form of the temperature distribution is obtained across the thickness of the beam as

$$\Theta_0 = \frac{\triangle_E}{\alpha_t \phi} \frac{\partial^2 W_0}{\partial x^2} \left(z - \frac{\sin\,(gz)}{g \cos\,\left(g\frac{h}{2}\right)} \right). \tag{4.1.25}$$

Substituting Eqs. (4.1.16) and (4.1.17) into Eq. (4.1.13), the equation of motion of the beam is deduced as follows:

$$\omega^2 W_0 = \frac{(EI)_{eq}}{\rho A} \left[1 + \frac{\triangle_E}{\Phi \Lambda} \left(1 + p(\omega)\right) \right] \frac{\partial^4 W_0}{\partial x^4}, \tag{4.1.26}$$

where

$$p(\omega) = \frac{24}{h^3 g^3} \left[\frac{hg}{2} - \tan\,\left(\frac{hg}{2}\right) \right]. \tag{4.1.27}$$

Also, $(EI)_{eq} = (EI + \mu A l^2)$ is equivalent stiffness and Λ is the rigidity ratio defined by

$$\Lambda = \frac{(EI)_{eq}}{EI} = 1 + 12\frac{\mu}{E}\left(\frac{l}{h}\right)^2. \tag{4.1.28}$$

Because of the fact that the thermoelastic coupling effect is very small, Eq. (4.1.26) can be written as follows:

$$\omega_0^2 W_0 = \frac{(EI)_{eq}}{\rho A} \frac{\partial^4 W_0}{\partial x^4}, \tag{4.1.29}$$

where $\omega_0 = p_n^2 \sqrt{\left(\frac{EI + \mu A l^2}{\rho A}\right)}$ is a size-dependent isothermal frequency, $p_n L = (4.73, 7.853,$ $10.996, ...)$, $n = 1, 2, 3$ for clamped-clamped boundary conditions at both ends of the beam.

By the virtue of Eqs. (4.1.26) and (4.1.29), the relationship between ω_0 and ω is found

as follows:

$$\omega = \omega_0 \sqrt{1 + \frac{\triangle_E \left(1 + p(\omega)\right)}{\Phi\Lambda}}. \tag{4.1.30}$$

Now, it is well known that the relaxation strength $\triangle_E << 1$. Hence, Taylor's series of the above relation is expanded up to first order term as follows:

$$\omega = \omega_0 \left[1 + \frac{\triangle_E}{2} \frac{\left(1 + p(\omega)\right)}{\Phi\Lambda}\right]. \tag{4.1.31}$$

Clearly, the difference between the magnitude of real and imaginary parts of $p(\omega)$ and $p(\omega_0)$ is very small (Borjalilou et al. (2019)). Therefore, the amount of thermoelastic damping is very weak and $p(\omega)$ can be replaced by $p(\omega_0)$. Therefore, the following is obtained:

$$\omega = \omega_0 \left[1 + \frac{\triangle_E}{2} \frac{\left(1 + p(\omega_0)\right)}{\Phi\Lambda}\right]. \tag{4.1.32}$$

The amount of the TED is expressed as the inverse of the QF (Lifshitz and Roukes (2000), Zener (1938)) given by

$$Q^{-1} = 2 \left| \frac{\text{Im } (\omega)}{\text{Re } (\omega)} \right|, \tag{4.1.33}$$

where Im (ω) represents attenuation of vibration and Re (ω) gives the new eigen frequencies of the beam resonator in the presence of thermoelastic coupling. Therefore, TED of the micro-beam on the basis of MCST theory and the Quintanilla Moore-Gibson-Thompson (MGT) thermoelasticity theory is finally derived in the closed form as

$$Q^{-1} = 24 \frac{\triangle_E}{\Phi\Lambda} \left[\frac{\beta_2}{\xi^2 \left(\xi_1^2 + \frac{\beta_2^2}{\xi_1^2}\right)^2} - \frac{\left\{ \left(3\xi_1\beta_2 - \frac{\beta_2^3}{\xi_1^3}\right) \sin\ (\xi\xi_1) - \left(\xi_1^3 - 3\frac{\beta_2^2}{\xi_1}\right) \sin\ \left(\xi\frac{\beta_2}{\xi_1}\right) \right\}}{\xi^3 \left(\xi_1^2 + \frac{\beta_2^2}{\xi_1^2}\right)^3 \left(\cos\ (\xi\xi_1) + \cosh\ \left(\xi\frac{\beta_2}{\xi_1}\right) \right)} \right]. \tag{4.1.34}$$

4.1.5 Numerical results and discussion

In this subsection, the impact of the essential parameters such as dimensionless parameter ξ, aspect ratio $(\frac{L}{h})$, and the relaxation parameter $\tau_q (10^{-10} \leq \tau_q \leq 10^{-8})$ on

the quality factor (QF) of size-dependent beam resonators are investigated with the help of numerical results. For the validation of the present analytical solutions, the results obtained here are also compared with the corresponding results of the special cases that are available in the literature (i.e. for classical continuum theory, LS, and GN-III models). The graphs are plotted for the variation of the inverse quality factor (Q^{-1}) scaled by relaxation strength ($\triangle_E$) i.e. $Q^{-1}/\triangle_E$ with respect to normalized frequency (ξ) and beam thickness (h). The utility of the present work for resonator design considering Silicon material is illustrated. The computational work is carried out by using MatLab and the results are shown in various figures. The considered properties of Silicon micro-beam at reference temperature $T_0 = 300K$ are listed in Table 4.1 (Tzou (2014)).

Material properties for Silicon	Values
Poisson's ratio (ϑ)	0.22
Mass density (ρ)	2330 kg/m^3
Specific heat at constant volume (c_E)	713 Jkg^{-1}K^{-1}
Young's modulus (E)	169 GPa
Thermal conductivity (K)	70 Wm^{-1}K^{-1}
Thermal conductivity rate (K^*)	157 Wm^{-1}K^{-1}s^{-1}
Thermal expansion coefficient (α_t)	2.6×10^{-6} K^{-1}

Table 4.1: Material properties for Silicon micro-beam

The influence of material length scale parameter (l) on size-dependent TED (scaled by $\triangle_E$) versus normalized frequency ξ is shown in Figs. 4.1.2(a,b). We show the results for different aspect ratios $\frac{L}{h} = 25$ and $\frac{L}{h} = 40$ with fixed thickness of the beam as $h = 1\,\mu m$. It is observed that in cases of both the theories (i.e., the classical continuum theory and MCST) under MGT model, the damping factor ($Q^{-1}/\triangle_E$) attains its peak values at the same critical frequency $\xi = 2.25$. However, it is important to note that the MCST calculates less values of TED than those of the CCT (classical continuum theory). This effect is more significant for lower values of aspect ratio (see Figs. 4.1.2(a,b)). It is further observed that although the predicted results have a sim-

ilar pattern for both classical continuum and modified couple stress theories when the MGT heat conduction equation is applied, however there is a pronounced influence of the material length parameter on TED under MCST and MGT theory, and enhancing in the value of QF under MCST can be achieved by increasing the length-scale parameter. The influence is more significant for higher values of aspect ratio. Thus, the QF of the beam resonator's sensitivity under MCST for MGT heat conduction theory is better in comparison to the case of CCT. Moreover, TED for MCST can occur for a longer time than CCT because of its lower energy dissipation rate.

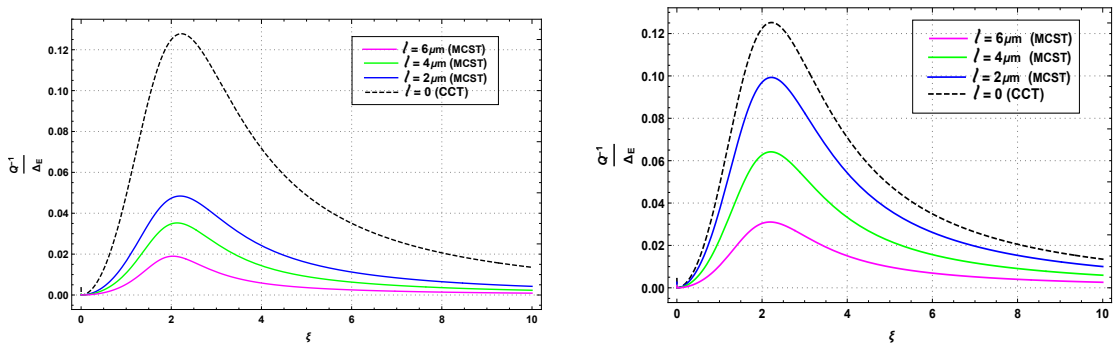

Figure 4.1.2: Variation of the damping factor $(Q^{-1}/\triangle_E)$ for various values of material length scale parameter l with aspect ratio (a) $\frac{L}{h} = 25$ (b) $\frac{L}{h} = 40$.

Fig. 4.1.3 depicts the fluctuation of the normalized frequency shift $\left(\frac{1}{\triangle_E}\frac{(Re(\omega)-\omega_0)}{\omega_0}\right)$ and the normalized attenuation $\left(\frac{1}{\triangle_E}\frac{\mathrm{Im}(\omega)}{\omega_0}\right)$ with respect to the normalized frequency (ξ) for fixed aspect ratio 25. Here, the variation is examined for fixed beam thickness $h = 1\,\mu m$. Notably, the normalized attenuation reaches a peak value at the critical frequency $\xi = 2.25$ and thereafter it tends to zero with the increase in frequency value. The normalized frequency shift increases with the increase of frequency and finally attains a constant limiting value. Also normalized frequency shift intersects with the normalized attenuation near the critical frequency, $\xi = 2.25$. This type of analogous behavior for other thermoelastic model has been reported by Lifshitz and Roukes (2000).

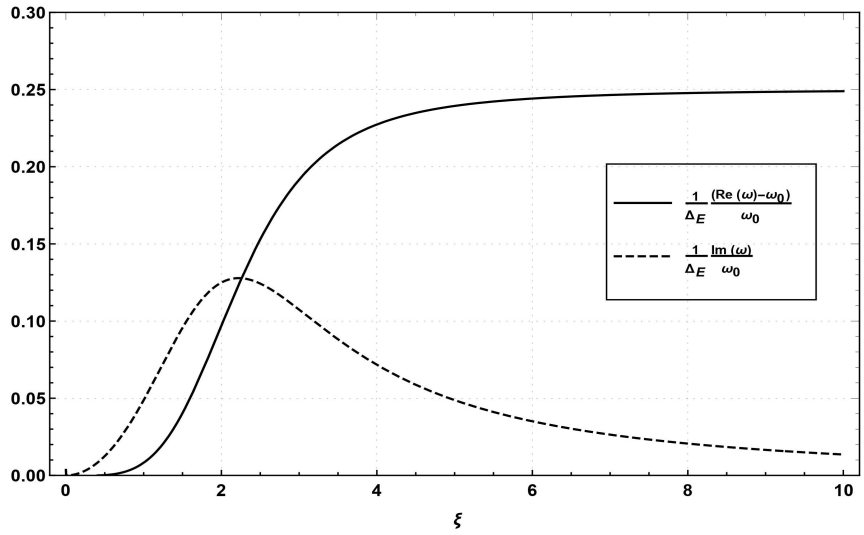

Figure 4.1.3: Fluctuation of normalized frequency shift $\frac{1}{\triangle_E}\frac{(Re(\omega)-\omega_0)}{\omega_0}$ and normalized attenuation $\frac{1}{\triangle_E}\left(\frac{Im(\omega)}{\omega_0}\right)$ versus the function of normalized frequency ξ.

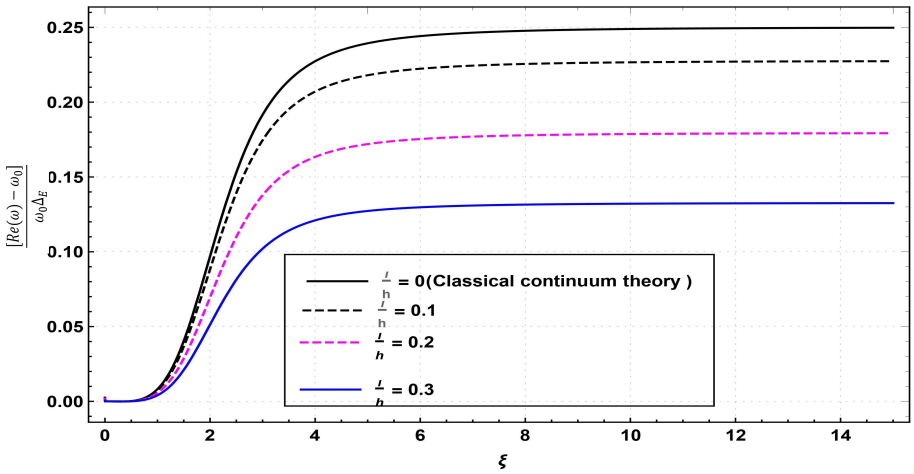

Figure 4.1.4: Variation of normalized frequency shift $\frac{1}{\triangle_E}\left[\frac{(Re(\omega)-\omega_0)}{\omega_0}\right]$ with the normalized frequency (ξ)

Fig. 4.1.4 displays the global behavior of normalized frequency shift $\left(\frac{\mathrm{Re}(\omega)-\omega_0}{\omega_0\triangle_E}\right)$ with respect to dimensionless variable ξ for fixed micro-beam thickness $h = 10^{-6}\,m$

and relaxation parameter $\tau_q = 0.388 \times 10^{-9}$ under both theories (MCST and CCT) for MGT thermoelastic model. The variation of normalized frequency shift for different aspect ratios $(\frac{l}{h})$ with length-scale parameter l has been plotted. It has been observed that with the increase in the aspect ratio $\frac{l}{h}$, the maximum amount (peak value) of TED for normalized frequency shift decreases significantly. Therefore, it is concluded that MCST with MGT theory predict smaller values of TED, implying a higher QF of the beam as compared to the case of CCT.

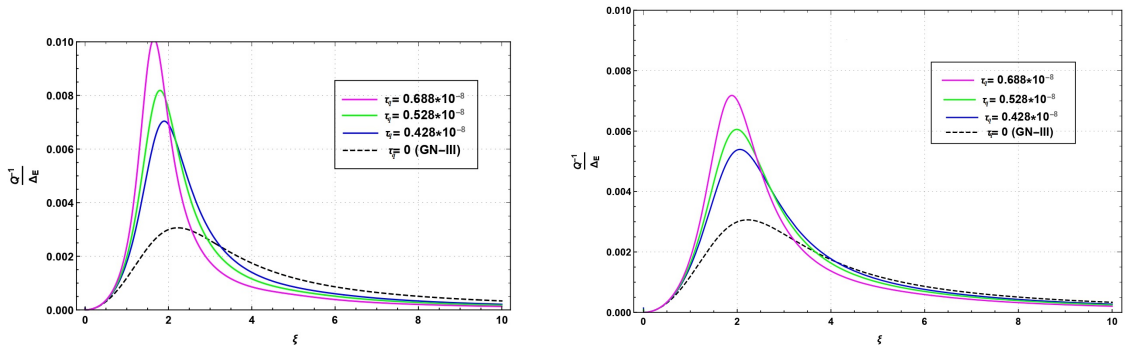

Figure 4.1.5: Variation of the damping factor $(Q^{-1}/\triangle_E)$ for different relaxation parameter (τ_q) with aspect ratio (a) $\frac{L}{h} = 40$ (b) $\frac{L}{h} = 50$.

The TED of the micro-beam against normalized frequency ξ is illustrated for different relaxation time parameter τ_q in Figs. 4.1.5(a,b) of the MGT theory. The length-scale parameter $l = 2\,\mu m$ is taken in the numerical computation for two aspect ratios, $L/h = 40$ and $L/h = 50$. It is observed that thermoelastic damping tends to its maximum peak as the value of the dimensionless variable ξ increases and after showing a peak value, it starts decreasing. The peak value is reached more quickly in the case of the MGT model as compared to GN-III model. Hence, it is noteworthy that the effect of the time relaxation parameter has a dominant impact on the micro-beam's inverse QF. Overall, one can conclude that the GN–III model has a maximum QF to allow the beam resonator oscillate for a longer time than this newly proposed model. It can be further concluded that the maximum QF can be obtained at lower values of relaxation

parameter values which are close to zero. As the relaxation parameter gets higher, the TED gets higher and becomes a cause of predicting less value of quality factor. Hence, beam resonators with lower values of thermal relaxation parameter can perform more efficiently.

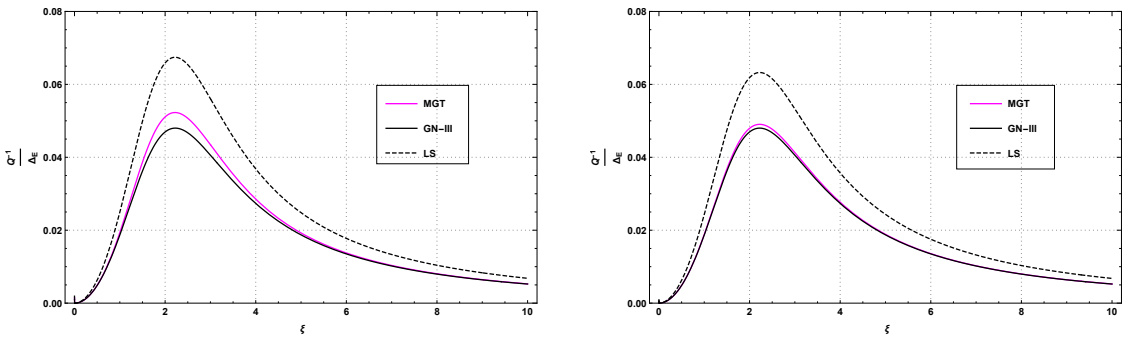

Figure 4.1.6: Variation of the damping factor ($Q^{-1}/\triangle_E$) for MGT, LS, and GN-III models with aspect ratio (a) $\frac{L}{h} = 20$ (b) $\frac{L}{h} = 40$.

Figs. 4.1.6(a,b) depict the variation of TED versus normalized frequency (ξ) based on three generalized theories, namely GN-III, MGT, and LS theories for the fixed value of length-scale parameter as $l = 0.4\,\mu m$ and for two different values of aspect ratio ($\frac{L}{h} = 20, 40$). Results are shown for the uniform micro thickness of the beam resonator and time relaxation parameter. It is seen that the thermoelastic damping predicted by the LS model has a large difference from the results predicted by MGT and GN-III theories. It can be clearly observed that by increasing the aspect ratio, the amount of TED decreases simultaneously and the behavior of TED for the MGT theory is close to the GN-III theory. It can be observed that the difference between MGT and the GN-III model becomes smaller with an increase of the ratio of beam length to beam thickness, $\frac{L}{h}$. Figs. 4.1.6(a,b) further demonstrate that the peak value of TED for the GN-III model does not change apparently, with the change of the aspect ratio $\frac{L}{h}$. However, the peak value of TED for MGT and LS models decreases as the aspect ratio increases. It is recognized that the variation of QF between LS and this results for other two theories

(GN-III and MGT) is considerable for both the aspect ratios. It can be noted that the high QF makes the micro-beam less flexible and increases its stability so that stable responses of the beam resonator can be observed. Thus, it is clear that dissipation of internal energy will occur slowly for MGT and GN-III models as compared to the LS model. Hence, the MGT heat conduction model predicts better results as compared to the Catteneo-Vernotte model.

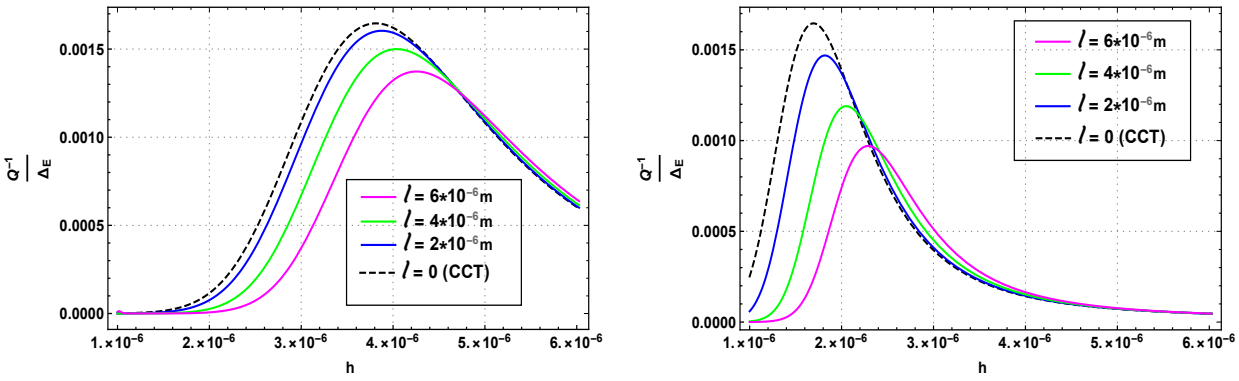

Figure 4.1.7: Variation of $\frac{Q^{-1}}{\triangle_E}$ against beam height h for CCT and MCST with aspect ratio (a) $\frac{L}{h} = 20$ (b) $\frac{L}{h} = 30$.

The dependency of the QF of vibration on the beam thickness (h) with different length-scale parameters l is plotted in Figs. 4.1.7(a,b). It is noted that the MCST gives a higher value of QF in comparison to those obtained by the CCT in both the plots. This implies that the rate of dissipation of energy is much higher in the case of CCT, so that the resonator will not sustain for a longer duration as compared to the MCST theory. There is also a prominent effect of the aspect ratio $\frac{L}{h}$. It is found that the increase in aspect ratio makes a sharp peak under both the theories (MCST and CCT) and the damping factor sharply decreases after attaining the peak value. Moreover, for the case of higher aspect ratios, the damping factor increases rapidly with the increase in the material length scale parameter and the peak values for both theories are attained at larger values of beam thickness. This is an important observation of the

present investigation and highlights the scope of designing beam resonators with better performance.

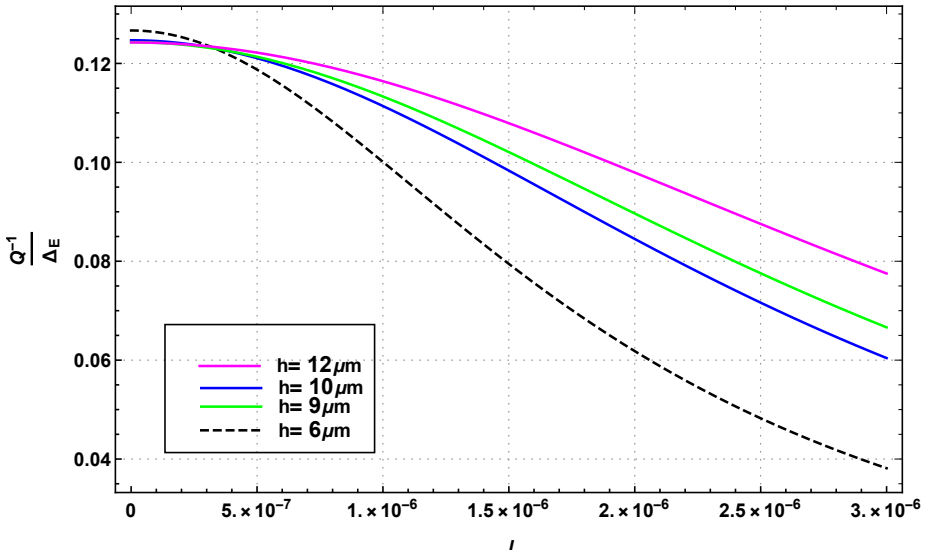

Figure 4.1.8: Variation of $\frac{Q^{-1}}{\triangle_E}$ with the length-scale parameter l for different values of beam thickness.

To illustrate the dependency on the material length-scale parameter, TED (scaled by the relaxation strength $\triangle_E$) for various values of a micro-beam thickness ($h = 6, 9, 10$ and $12\,\mu m$) is exhibited in Fig. 4.1.8. It is deduced that for $h = 9\,\mu m$, the value of nanobeam thickness possesses a lower QF than the value as determined at the beam thickness of $h = 10\,\mu m$. Furthermore, it can be seen that the peak value of TED is captured fairly at the critical thickness $h = 6\,\mu m$. Fig. 4.1.8 further demonstrates that the effect of beam thickness on TED is not monotone in nature for the present context. A similar type of prediction has been observed for dual phase-lag thermoelasticity as reported by Borjalilou and Mohsen Asghari (Borjalilou et al. (2019)).

4.1.6 Conclusion

The present investigation analyses the thermoelastic damping (TED) behavior in micro-beam resonators utilizing the modified couple stress theory (MCST) and the recently proposed thermoelasticity theory based on the Moore-Gibson-Thompson (MGT) heat

conduction equation. The coupled dynamical governing equation of motion is obtained by using the Hamilton principle. To analyze the prediction of the quality factor of micro-beam resonators in the present context and of the resonator's better quality performance, an attempt is made to illustrate the prominent impact of the new model on TED. After deriving the closed form analytical expression of the damping factor, the findings are illustrated through graphical results for a suitable material. The variation of TED have been compared and analyzed with those obtained by the classical continuum theory (CCT) and the modified couple stress theory (MCST) against dimensionless variable ξ, beam thickness h, and length-scale parameter l. The prediction of the new model is also compared with the same predicted by other thermoelastic models which were obtained as a special case of the present investigation. The conclusions arising out of the work can be highlighted as follows:

- The non-classical continuum theory (MCST) along with the MGT theory predicts a higher value of quality factor than the classical continuum theory for larger values of the material length scale parameter.

- The size-dependent normalized frequencies shift to lower values under the MCST, with the fixed beam thickness at the micro-scale.

- Intensifying relaxation parameter τ_q of MGT theory and reducing the aspect ratio of the beam cause a sharpening effect on TED. This implies that for a lower aspect ratio, the rate of energy dissipation is much higher.

- Under MCST and MGT theory, the TED does not show monotone behavior with the variation in the thickness of the beam.

- The result of quality factor under the GN-III model is considerably larger than those estimated by the MGT and LS models. However, the GN-III model and the new model show comparatively close predictions as compared to the LS model,

implying that the MGT heat conduction model can achieve higher performance of the micro-beam resonator as compared to the Catteneo-Vernotte heat conduction model.

4.2 Thermoelastic Vibration of Timoshenko Beam under the Modified Couple Stress Theory and Moore-Gibson-Thompson (MGT) Heat Conduction Model

4.2.1 Introduction[2]

Vibration analysis is typically performed using beams that are usually sub-micron and micron thick, which are commonly used in sensors and actuators. This inspired the design of Timoshenko beam models adopting higher-order continuum theories that include extra material constants. In this subchapter 4.2, the variational formulation of the micro structure-dependent Timoshenko beam model is developed considering Hamilton's principle and modified couple stress theory (MCST) in the context of the Moore-Gibson-Thompson (MGT) heat conduction model.

Many researchers have performed significant contributions to vibration analysis for thick Timoshenko beam. Ma et al. (2008) investigated micro-structure dependent Timoshenko beam model under the modified couple stress theory. In the framework of MCST, Asghari et al. (2010) evaluated a nonlinear formulation of the Timoshenko beam to represent the characteristics of both shear deformation and rotating inertia. In a subsequent study, Asghari et al. (2011) used the functionally graded Timoshenko beam to capture the size effect based on the MCST. The dynamical stability of a functionally graded non-classical Timoshenko beam was examined using MCST by Ke and Wang (2011). Roque et al. (2011) studied the Timoshenko nanobeams with a nonlocal formulation and meshless method. Analysis and modeling the size effect on vibration of functionally graded nanobeams based on nonlocal Timoshenko beam theory studied by Rahmani and Pedram (2014). Kumar (2020) established the formula for the dynamic deflection and thermal moment under the TPL heat conduction model. Recently, Ku-

[2]The content of this sub chapter is accepted in Mathematics and Mechanics of Solids (MMS), 2023.

mar and Mukhopadhyay (2021) constructed the mathematical and graphical responses of dimensionless deflection and thermal moment Timoshenko beam considering DPL heat conduction model.

It is evident that the governing equations for dynamic motion determined by the MCST and MGT heat conduction theories of a Timoshenko microbeam have not yet been developed. Subchapter 4.2 focuses on fulfilling this gap in the literature. This current work utilizes Hamilton's principle and includes axial and bending loads. The valid analytical formula for dimensionless deflection and normalized thermal moment is derived by using the Fourier series and the Laplace transform approach with the appropriate boundary conditions. The finding of the current subchapter 4.2 reveals that the MCST theory has a significantly higher energy dissipation rate due to deflection attenuation than the CCT theory.

4.2.2 Dynamic equations formulation of Timoshenko microbeam

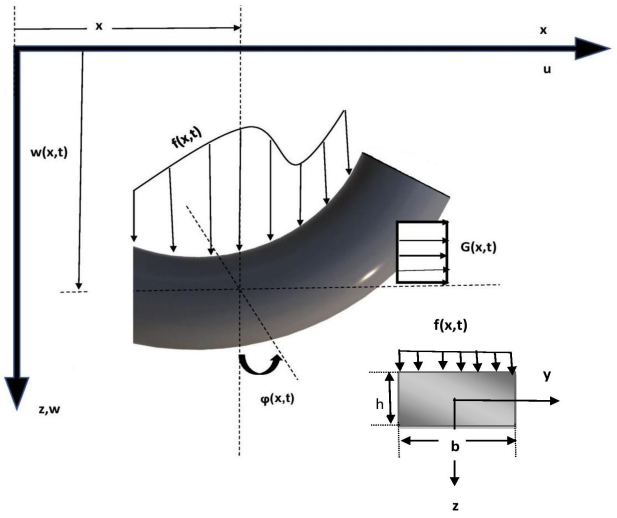

Figure 4.2.1: Coordinate system and loading of a deformed Timoshenko beam

4.2.2.1 Kinematic relations

Coordinate system of a rectangular microbeam with transverse distribution $f(x,t)$ and axial body load $G(x,t)$ per unit length is depicted in Fig. 4.2.1. The rectangular Timoshenko beam is considered with length L, width b and height h along the $x-, y-$ and $z-$ directions, respectivly. After a rigid body displacement in the $x-z$ plane, the displacement components of a deformed microbeam can be described as follows (Ma et al. (2008), Borjalilou et al. (2019)):

$$u_x = u(x,t) + z\varphi_x(x,t), \quad u_y = 0, \quad u_z = w(x,t), \tag{4.2.1}$$

where u_x, u_y, and u_z are the displacement components along x, y, and $z-$ directions, respectively. Also, φ_x is the angle of rotation of cross section with respect to vertical direction, y-axis. Moreover, the notations $u(x,t)$ and $w(x,t)$ stand for a beam's axial and transverse displacement, respectively. Indeed, it is supposed that all cross-sections stay plane after both transverse and axial loads but they may experience a rigid body displacement as well as rotation.

To develop the governing equations of motion with the help of strain energy, the non-zero components of strain tensor e_{ij} and volumetric strain e_{kk} are found firstly. Using Eq. (4.2.1), the non-zero components of strain tensor e_{ij} can be obtained as follows:

$$e_{xx} = \frac{\partial u}{\partial x} + z\frac{\partial \varphi_x}{\partial x}, \tag{4.2.2}$$

$$e_{xz} = e_{zx} = \frac{1}{2}\left(\varphi_x + \frac{\partial w}{\partial x}\right). \tag{4.2.3}$$

Therefore, the volumetric stain e_{kk} can be expressed as

$$e_{kk} = e_{xx} + e_{yy} + e_{zz} = \frac{\partial u}{\partial x} + z\frac{\partial \varphi_x}{\partial x}, \tag{4.2.4}$$

as $e_{yy} = e_{zz} = 0$. Also, the non-zero component of rotation vector v is as follows:

$$v_y = \frac{1}{2}\left(\varphi_x - \frac{\partial w}{\partial x}\right). \tag{4.2.5}$$

Further, the non-zero components of symmetrical part of curvature tensor is as

$$\chi_{xy} = \chi_{yx} = \frac{1}{4}\left(\frac{\partial \varphi_x}{\partial x} - \frac{\partial^2 w}{\partial x^2}\right). \tag{4.2.6}$$

It is notable that the beam's thickness h ($z-$direction) is very small in proportion to its length L ($x-$direction) and width b ($y-$direction). Therefore, axial strain in the $z-$direction (along thickness) e_{zz} is assumed to be zero. Because the width of the microbeam is sufficiently small as compared to its length L, it is possible to infer from the plane stress condition that the stress components in the width b direction are zero. By assuming the aforementioned explanation, the normal and shear stress components can be expressed as

$$\sigma_{xx} = Ee_{xx} - \beta\theta \text{ and } \sigma_{xz}{=}2\mu e_{xz}, \tag{4.2.7}$$

where $\beta = \frac{E\alpha_t}{(1-2\vartheta)}$. From Eq. (4.2.7), the non-zero components of the stress tensor can be calculated as follows:

$$\sigma_{xx} = E\left(\frac{\partial u}{\partial x} + z\frac{\partial \varphi_x}{\partial x}\right) - \beta\theta, \tag{4.2.8}$$

$$\sigma_{xz} = \sigma_{zx} = \mu\left(\varphi_x + \frac{\partial w}{\partial x}\right). \tag{4.2.9}$$

Also, the non-zero components of the couple stress tensor are obtained as

$$\Upsilon_{xy} = \Upsilon_{yx} = \frac{1}{2}\mu l^2\left(\frac{\partial \varphi_x}{\partial x} - \frac{\partial^2 w}{\partial x^2}\right). \tag{4.2.10}$$

4.2.2.2 Hamilton's principle for Timoshenko microbeam based on MCST

Hamilton's principle is used to get the equation of motion and related boundary conditions in this subsection. The strain energy due to bending can be expressed as (Kumar and Mukhopadhyay (2021))

$$U_s = \frac{1}{2}\int_0^L \int_A \left[\sigma_{xx}e_{xx} + \sigma_{xz}e_{xz} + \sigma_{zx}e_{zx} + \Upsilon_{xy}\chi_{xy} + \Upsilon_{yx}\chi_{yx}\right] dAdx. \tag{4.2.11}$$

Using Eqs. (4.2.8) – (4.2.10), the strain energy is obtained as

$$\begin{aligned} U_s = \frac{1}{2}\int_0^L \int_A \Bigg[& E\left(\frac{\partial u}{\partial x} + z\frac{\partial \varphi_x}{\partial x}\right)^2 - \beta\theta\left(\frac{\partial u}{\partial x} + z\frac{\partial \varphi_x}{\partial x}\right) \\ & + \mu\left(\varphi_x + \frac{\partial w}{\partial x}\right)^2 + \frac{\mu l^2}{4}\left(\frac{\partial \varphi_x}{\partial x} - \frac{\partial^2 w}{\partial x^2}\right)^2\Bigg] dAdx. \end{aligned} \tag{4.2.12}$$

Moreover, the kinetic energy of beam is given by (Ma et al. (2008))

$$\begin{aligned} \hat{\Upsilon}_{K.E} &= \frac{1}{2}\int_V \rho\left[\left(\frac{\partial u_x}{\partial t}\right)^2 + \left(\frac{\partial u_y}{\partial t}\right)^2 + \left(\frac{\partial u_z}{\partial t}\right)^2\right] dV \\ &= \frac{1}{2}\int_0^L \int_A \rho\left[\left(\frac{\partial u}{\partial t} + z\frac{\partial \varphi_x}{\partial t}\right)^2 + \left(\frac{\partial w}{\partial t}\right)^2\right] dAdx, \end{aligned} \tag{4.2.13}$$

Now, we introduce the following components:

$$I = \frac{bh^3}{12}, \quad m_1 = \int_A \rho dA, \quad m_2 = \int_A \rho z^2 dA, \tag{4.2.14}$$

and

$$I_1 = \int_A \beta\theta z dA = b\int_{-h/2}^{h/2} \beta\theta z dz, \tag{4.2.15}$$

$$I_2 = \int_A \beta\theta dA = b\int_{-h/2}^{h/2} \beta\theta dz, \tag{4.2.16}$$

where I, ρ refer the moment of inertia of cross section and density of microbeam, respectively. Also, I_1 and I_2 indicate resultants of thermal moments.
The variation in work done by external forces in the deformed beam can be expressed as (Kumar and Mukhopadhyay (2021), Kumar (2020))

$$\delta W = \int_0^L f(x,t)w(x,t)dx + \int_0^L G(x,t)u(x,t)dx + \left(\hat{N}_f u(x,t)\right)\Big|_{x=0}^{x=L} + \left(\hat{V}_f w(x,t)\right)\Big|_{x=0}^{x=L} + \left(\hat{M}_s \varphi_x\right)\Big|_{x=0}^{x=L} + \left(\hat{M}_a v_y\right)\Big|_{x=0}^{x=L}, \tag{4.2.17}$$

where $\hat{N}_f$ and $\hat{V}_f$ represent the resultant forces in axial and transverse direction cased by classical stresses, respectively. Here, $\hat{M}_s$ symbolizes the resultant moment in an end section induced by classical stress σ_{ij} and v_y indicates component of rotation vector. The parameter $\hat{M}_a$ is resultant bending moment caused by the higher order stress Υ_{ij}.

For a system with predefined configurations at $t_1 \leq t \leq t_2$, the Hamilton's principle states that actual motion minimizes the difference between kinetic energy and total potential energy. The application of Hamilton's principle can be expressed as

$$\delta \int_{t_1}^{t_2} \left(\hat{\Upsilon}_{K.E} - U_s + W\right) dt = 0. \tag{4.2.18}$$

In view of the above principle, we obtain the governing equations of motion and corresponding boundary conditions when we set the coefficients of δu, $\delta\varphi_x$ and δw to be zero. Therefore, in the virtue of Eqs. (4.2.12), (4.2.13), (4.2.17) and (4.2.18), we obtain the governing equations of moion as

$$\delta u: \ \frac{\partial}{\partial x}\left[-(EA)\frac{\partial u}{\partial x} + \frac{I_2}{2}\right] = -m_1\left(\frac{\partial^2 u}{\partial t^2}\right) + G(x,t), \tag{4.2.19}$$

$$\delta\varphi_x: \ -\left[(EI) + \left(\frac{\mu A l^2}{4}\right)\right]\left(\frac{\partial^2 \varphi_x}{\partial x^2}\right) + (\mu A)\left(\varphi_x + \frac{\partial w}{\partial x}\right) + \left(\frac{\mu A l^2}{4}\right)\left(\frac{\partial^3 w}{\partial x^3}\right) + \frac{1}{2}\left(\frac{\partial I_1}{\partial x}\right) = -m_2\left(\frac{\partial^2 \varphi_x}{\partial t^2}\right), \tag{4.2.20}$$

$$\delta w: \; -(\mu A)\frac{\partial}{\partial x}\left[\varphi_x+\frac{\partial w}{\partial x}+\left(\frac{l^2}{4}\right)\left(\frac{\partial^2\varphi_x}{\partial x^2}-\frac{\partial^3 w}{\partial x^3}\right)\right] \tag{4.2.21}$$
$$=-m_1\left(\frac{\partial^2 w}{\partial t^2}\right)+f(x,t).$$

Also, the pertinent boundary conditions at associated edges $x=0$ and $x=L$ are taken as (Kumar and Mukhopadhyay (2021))

$$\left[(EA)\left(\frac{\partial u}{\partial x}\right)-\left(\frac{I_2}{2}\right)\right]=\hat{N}_f \;\text{ or }\; \delta u=0, \tag{4.2.22}$$

$$\left[(EI)+\left(\frac{\mu A l^2}{4}\right)\right]\left(\frac{\partial\varphi_x}{\partial x}\right)-\left(\frac{\mu A l^2}{4}\right)\left(\frac{\partial^2 w}{\partial x^2}\right)-\left(\frac{I_1}{2}\right)=M_s+\frac{\hat{M}_a}{2} \;\text{ or }\; \delta\varphi_x=0, \tag{4.2.23}$$

$$(\mu A)\left[\varphi_x+\frac{\partial w}{\partial x}+\left(\frac{l^2}{4}\right)\left(\frac{\partial^2\varphi_x}{\partial x^2}-\frac{\partial^3 w}{\partial x^3}\right)\right]=\hat{V}_f \;\text{ or }\; \delta w=0, \tag{4.2.24}$$

$$\left(\frac{\mu A l^2}{2}\right)\left(\frac{\partial^2 w}{\partial x^2}-\frac{\partial\varphi_x}{\partial x}\right)=-\hat{M}_a \;\text{ or }\; \delta\left(\frac{\partial w}{\partial x}\right)=0. \tag{4.2.25}$$

4.2.3 Heat conduction equation for microbeam

By neglecting the presence of any external heat source, the MGT heat conduction equation takes following form (see Eq. 4.1.9 of Chapter 4.1):

$$\left(K\frac{\partial}{\partial t}+K^*\right)\left(\frac{\partial^2\theta}{\partial x^2}+\frac{\partial^2\theta}{\partial z^2}\right)-\left(1+\tau_q\frac{\partial}{\partial t}\right)\left(\rho c_E\frac{\partial^2\theta}{\partial t^2}+T_0\beta\frac{\partial^2 e_{kk}}{\partial t^2}\right)=0, \tag{4.2.26}$$

where $e_{kk}=\frac{\partial u}{\partial x}+z\frac{\partial\varphi_x}{\partial x}$.

From Eq. (4.2.26), one can obtain

$$\left(K\frac{\partial}{\partial t}+K^*\right)\left(\frac{\partial^2\theta}{\partial x^2}+\frac{\partial^2\theta}{\partial z^2}\right)-\left(1+\tau_q\frac{\partial}{\partial t}\right)\left[\rho c_E\frac{\partial^2\theta}{\partial t^2}+T_0\beta\left(\frac{\partial^3 u}{\partial t^2\partial x}+z\frac{\partial^3\varphi_x}{\partial t^2\partial x}\right)\right]=0. \tag{4.2.27}$$

Alternatively, multiplying Eq. (4.2.27) by $b\beta z$ and integrating with respect to z from $-\frac{h}{2}$ to $\frac{h}{2}$, it is obtained that

$$\left(K\frac{\partial}{\partial t}+K^{*}\right)\left(\frac{\partial^{2}I_{1}}{\partial x^{2}}+b\beta\int_{-h/2}^{h/2}z\frac{\partial^{2}\theta}{\partial z^{2}}dz\right)-\left(1+\tau_{q}\frac{\partial}{\partial t}\right)\left[\rho c_{E}\frac{\partial^{2}I_{1}}{\partial t^{2}}+IT_{0}\beta^{2}\frac{\partial^{3}\varphi_{x}}{\partial t^{2}\partial x}\right]=0. \tag{4.2.28}$$

The temperature along the beam thickness direction ($z-$direction) is supposed to vary in term of sin (gz) function. Therefore, putting $\theta\left(x,z,t\right)=\widetilde{\theta}\left(x,t\right)\sin(gz)$ and $g=\pi/h$ into Eq. (4.2.28), yields

$$\left(K\frac{\partial}{\partial t}+K^{*}\right)\left(\frac{\partial^{2}I_{1}}{\partial x^{2}}-g^{2}I_{1}\right)=\left(1+\tau_{q}\frac{\partial}{\partial t}\right)\left[\rho c_{E}\frac{\partial^{2}I_{1}}{\partial t^{2}}+IT_{0}\beta^{2}\frac{\partial^{3}\varphi_{x}}{\partial t^{2}\partial x}\right], \tag{4.2.29}$$

where

$$I_{1}=-\frac{1}{g^{2}}\int_{-h/2}^{h/2}b\beta z\frac{\partial^{2}\widetilde{\theta}}{\partial z^{2}}dz.$$

Using Eqs. $(4.2.19)-(4.2.21)$ and Eq. (4.2.29), the coupled governing equations in the context of MCST are found as

$$\delta u:\ -E\left(\frac{\partial^{2}u}{\partial x^{2}}\right)=-\rho\left(\frac{\partial^{2}u}{\partial t^{2}}\right)+\frac{G(x,t)}{A}, \tag{4.2.30}$$

$$\begin{aligned}\delta\varphi_{x}:\ &-M\left(\frac{\partial^{2}\varphi_{x}}{\partial x^{2}}\right)+\left(\frac{\mu}{n_{x}^{2}}\right)\left(\varphi_{x}+\frac{\partial w}{\partial x}\right)+\left(\frac{\mu}{4}\right)\left(\frac{l}{n_{x}}\right)^{2}\left(\frac{\partial^{3}w}{\partial x^{3}}\right)+\frac{1}{2I}\left(\frac{\partial I_{1}}{\partial x}\right)\\&=-\rho\left(\frac{\partial^{2}\varphi_{x}}{\partial t^{2}}\right),\end{aligned} \tag{4.2.31}$$

$$\delta w:\ -\mu\frac{\partial}{\partial x}\left[\varphi_{x}+\frac{\partial w}{\partial x}+\left(\frac{l^{2}}{4}\right)\left(\frac{\partial^{2}\varphi_{x}}{\partial x^{2}}-\frac{\partial^{3}w}{\partial x^{3}}\right)\right]=-\rho\left(\frac{\partial^{2}w}{\partial t^{2}}\right)+\frac{f\left(x,t\right)}{A}, \tag{4.2.32}$$

$$\left(K\frac{\partial}{\partial t}+K^{*}\right)\left(\frac{\partial^{2}I_{1}}{\partial x^{2}}-r^{2}I_{1}\right)=\left(1+\tau_{q}\frac{\partial}{\partial t}\right)\left[\rho c_{E}\frac{\partial^{2}I_{1}}{\partial t^{2}}+IT_{0}\beta^{2}\frac{\partial^{3}\varphi_{x}}{\partial t^{2}\partial x}\right], \tag{4.2.33}$$

where $M=E+\left(\frac{\mu}{4}\right)\left(\frac{l}{n_x}\right)^{2}$ and $n_x=\sqrt{\frac{I}{A}}=\frac{h}{2\sqrt{3}}$ is radius of gyration of body about the axis of rotation.

Boundary conditions at both end $x=0$ and $x=L$ are reduced in simplified forms as

$$E\left(\frac{\partial u}{\partial x}\right)=\frac{\hat{N}_{f}}{A}\quad\text{or}\quad\delta u=0, \tag{4.2.34}$$

$$M\left(\frac{\partial\varphi_{x}}{\partial x}\right)-\left(\frac{\mu}{4}\right)\left(\frac{l}{n_x}\right)^{2}\left(\frac{\partial^{2}w}{\partial x^{2}}\right)-\frac{I_{1}}{2I}=\frac{M_{s}+\frac{\hat{M}_{a}}{2}}{I}\quad\text{or}\quad\delta\varphi_{x}=0, \tag{4.2.35}$$

$$\mu\left[\varphi_{x}+\frac{\partial w}{\partial x}+\left(\frac{l^{2}}{4}\right)\left(\frac{\partial^{2}\varphi_{x}}{\partial x^{2}}-\frac{\partial^{3}w}{\partial x^{3}}\right)\right]=\frac{\hat{V}_{f}}{A}\quad\text{or}\quad\delta w=0, \tag{4.2.36}$$

$$\left(\frac{\mu l^{2}}{2}\right)\left(\frac{\partial^{2}w}{\partial x^{2}}-\frac{\partial\varphi_{x}}{\partial x}\right)=-\frac{\hat{M}_{a}}{A}\quad\text{or}\quad\delta\left(\frac{\partial w}{\partial x}\right)=0. \tag{4.2.37}$$

The following dimensionless quantities are defined to simplify above coupled thermoelastic equations:

$$x'=\frac{x}{L},\ \ \tau'=\frac{t\epsilon}{L},\ \ \epsilon=\sqrt{\frac{E}{\rho}},\ \ \varphi=\varphi_{x},\ \ u'=\frac{u}{h},\ \ \Omega=\frac{w}{h},\ \ \tau_{1}=\frac{\tau_{q}\epsilon}{L},\ \ \Phi=\frac{I_{1}}{EAh}, \tag{4.2.38}$$

where Ω and Φ stand for dimensionless deflection and thermal moment, respectively. Here, u' and φ are the axial displacement and rotation angle of cross-section of beam, respectively.

Eqs. (4.2.38) and (4.2.29) – (4.2.33) provide the following non-dimensional forms (dropping the primes for simplicity):

$$\delta u:\ -\left(\frac{\partial^{2}u}{\partial x^{2}}\right)=-\left(\frac{\partial^{2}u}{\partial\tau^{2}}\right)+G^{*}, \tag{4.2.39}$$

$$\delta\varphi: \ -C_1\left(\frac{\partial^2\varphi}{\partial x^2}\right)+C_2\varphi-C_3\left(\frac{\partial^3\Omega}{\partial x^3}\right)+C_4\left(\frac{\partial\Omega}{\partial x}\right)+C_5\left(\frac{\partial\Phi}{\partial x}\right)=-\rho\left(\frac{\partial^2\varphi}{\partial\tau^2}\right), \tag{4.2.40}$$

$$\delta\Omega: \ C_6\left(\frac{\partial^3\varphi}{\partial x^3}\right)-C_7\left(\frac{\partial\varphi}{\partial x}\right)+C_8\left(\frac{\partial^4\Omega}{\partial x^4}\right)-C_9\left(\frac{\partial^2\Omega}{\partial x^2}\right)=-\left(\frac{\partial^2\Omega}{\partial\tau^2}\right)+f^*, \tag{4.2.41}$$

$$\left(p_0+\frac{\partial}{\partial\tau}\right)\left(\frac{\partial^2\Phi}{\partial x^2}-C_{10}\Phi\right)-\left(1+\tau_1\frac{\partial}{\partial\tau}\right)\left(C_{11}\frac{\partial^2\Phi}{\partial\tau^2}+C_{12}\left(\frac{\partial^3\varphi}{\partial\tau^2\partial x}\right)\right)=0, \tag{4.2.42}$$

where

$$p_0=\frac{K^*L}{K\epsilon}, \quad G^*=\frac{G\left(x,t\right)}{\frac{EAh}{L^2}}, \quad f^*=\frac{f\left(x,t\right)}{\frac{EAh}{L^2}}.$$

At the constant temperature, the simply supported microbeam is considered with constant force per unit length i.e., $f(x,t)=f_0\delta(t)$. It is assumed that there is no axial body force i.e., $G\left(x,t\right)=0$. Then, the coupled thermoelastic equations are derived as follows:

$$\delta u: \ \frac{\partial^2 u}{\partial x^2}=\left(\frac{\partial^2 u}{\partial\tau^2}\right), \tag{4.2.43}$$

$$\begin{aligned}\delta\varphi: \ &-C_1\left(\frac{\partial^2\varphi}{\partial x^2}\right)+C_2\varphi-C_3\left(\frac{\partial^3\Omega}{\partial x^3}\right)+C_4\left(\frac{\partial\Omega}{\partial x}\right)+C_5\left(\frac{\partial\Phi}{\partial x}\right)=-\left(\frac{\partial^2\varphi}{\partial\tau^2}\right),\\ &+C_5\left(\frac{\partial\Phi}{\partial x}\right)=-\left(\frac{\partial^2\varphi}{\partial\tau^2}\right),\end{aligned} \tag{4.2.44}$$

$$\begin{aligned}\delta\Omega: \ &C_6\left(\frac{\partial^3\varphi}{\partial x^3}\right)-C_7\left(\frac{\partial\varphi}{\partial x}\right)+C_8\left(\frac{\partial^4\Omega}{\partial x^4}\right)-C_9\left(\frac{\partial^2\Omega}{\partial x^2}\right)\\ &=-\left(\frac{\partial^2\Omega}{\partial\tau^2}\right)+f_0^*\delta(\tau),\end{aligned} \tag{4.2.45}$$

$$\left(p_0+\frac{\partial}{\partial\tau}\right)\left(\frac{\partial^2\Phi}{\partial x^2}-C_{10}\Phi\right)-\left(1+\tau_1\frac{\partial}{\partial\tau}\right)\left(C_{11}\frac{\partial^2\Phi}{\partial\tau^2}+C_{12}\left(\frac{\partial^3\varphi}{\partial\tau^2\partial x}\right)\right)=0, \tag{4.2.46}$$

where $f_0^*=\frac{f_0L^2}{EAh}$.

It is considered that the supports at edges of beam exhibits no deflection. It is also

expected that the supports at the microbeam's edges do not generate any bending moment. Therefore, the pertinent initial and boundary conditions are taken in the following way:

$$
\begin{aligned}
&u\big|_{\tau=0} = \frac{\partial u}{\partial \tau}\big|_{\tau=0} = 0, \quad \varphi\big|_{\tau=0} = \frac{\partial \varphi}{\partial \tau}\big|_{\tau=0} = 0, \\
&\Omega\big|_{\tau=0} = \frac{\partial \Omega}{\partial \tau}\big|_{\tau=0} = 0, \quad \Phi\big|_{\tau=0} = \frac{\partial \Phi}{\partial \tau}\big|_{\tau=0} = 0, \qquad (4.2.47) \\
&u\big|_{x=0}^{x=1} = \frac{\partial^2 u}{\partial x^2}\bigg|_{x=0}^{x=1} = 0, \quad \left(C_1\left(\frac{\partial \varphi}{\partial x}\right) + C_3\left(\frac{\partial^2 \Omega}{\partial x^2}\right) - C_5\left(\Phi\right)\right)\bigg|_{x=0}^{x=1} = \left(\frac{\partial \varphi}{\partial x}\right)\bigg|_{x=0}^{x=1} = 0, \\
&\Omega\bigg|_{x=0}^{x=1} = C_6\left(\frac{\partial \varphi}{\partial x}\right) + C_8\left(\frac{\partial^2 \Omega}{\partial x^2}\right)\bigg|_{x=0}^{x=1} = 0, \quad \Phi\bigg|_{x=0}^{x=1} = 0. \qquad (4.2.48)
\end{aligned}
$$

4.2.4 Solution of the problem

In this subsection, the Laplace transform technique is employed to solve Eqs. (4.2.44) – (4.2.46) with the initial conditions (4.2.47).
Therefore, it is obtained that

$$
\begin{aligned}
\overline{\varphi}\left(x,p\right) &= \int_0^\infty \varphi\left(x,\tau\right) e^{-p\tau} d\tau, \\
\overline{\Omega}\left(x,p\right) &= \int_0^\infty \Omega\left(x,\tau\right) e^{-p\tau} d\tau, \qquad (4.2.49) \\
\overline{\Phi}\left(x,p\right) &= \int_0^\infty \Phi\left(x,\tau\right) e^{-p\tau} d\tau.
\end{aligned}
$$

Here, p is the Laplace transform parameter.
By the virtue of Eq. (4.2.49) and applying homogeneous initial conditions (4.2.47), the coupled thermoelastic Eqs. (4.2.44) – (4.2.46) can be written as

$$
\begin{aligned}
-C_1\left(\frac{\partial^2 \overline{\varphi}\left(x,p\right)}{\partial x^2}\right) + \left(C_2 + p^2\right)\overline{\varphi}\left(x,p\right) - C_3\left(\frac{\partial^3 \overline{\Omega}\left(x,p\right)}{\partial x^3}\right) \\
+C_4\left(\frac{\partial \overline{\Omega}\left(x,p\right)}{\partial x}\right) + C_5\left(\frac{\partial \overline{\Phi}\left(x,p\right)}{\partial x}\right) = 0, \qquad (4.2.50)
\end{aligned}
$$

$$C_6\left(\frac{\partial^3\overline{\varphi}\left(x,p\right)}{\partial x^3}\right)-C_7\left(\frac{\partial\overline{\varphi}\left(x,p\right)}{\partial x}\right)+C_8\left(\frac{\partial^4\overline{\Omega}\left(x,p\right)}{\partial x^4}\right)$$
$$-C_9\left(\frac{\partial^2\overline{\Omega}\left(x,p\right)}{\partial x^2}\right)+p^2\overline{\Omega}\left(x,p\right)-f_0^*=0, \tag{4.2.51}$$
$$\left(p_0+p\right)\left(\frac{\partial^2\overline{\Phi}\left(x,p\right)}{\partial x^2}-C_{10}\overline{\Phi}\left(x,p\right)\right)-\left(1+\tau_1 p\right)\left(C_{11}p^2\overline{\Phi}\left(x,p\right)\right.$$
$$\left.+C_{12}p^2\left(\frac{\partial\overline{\varphi}\left(x,p\right)}{\partial x}\right)\right)=0. \tag{4.2.52}$$

In order to write the basic kinematic functions in the dynamic analysis, one can use the Fourier series, which are appropriate with the boundary conditions specified by Eq. (4.2.48).

By employing the Fourier series, the following equations are obtained:

$$\begin{aligned}\overline{\varphi}\left(x,p\right)&=\sum_{m=1}^{\infty}\overline{\varphi}_m\left(p\right)\cos(m\pi x),\\ \overline{\Omega}\left(x,p\right)&=\sum_{m=1}^{\infty}\overline{\Omega}_m\left(p\right)\sin(m\pi x),\\ \overline{\Phi}\left(x,p\right)&=\sum_{m=1}^{\infty}\overline{\Phi}_m\left(p\right)\sin(m\pi x).\end{aligned} \tag{4.2.53}$$

Also, the normalized constant force f_0^* can be taken as

$$f_0^*=\sum_{m=1}^{\infty}F_m\sin(m\pi x)\,, \tag{4.2.54}$$

where

$$F_m=2\int_0^1 f_0^*\sin(m\pi x)dx=\frac{4f_0^*}{m\pi},\quad m=(1,3,5....)\,.$$

Putting Eqs. (4.2.53) and (4.2.54) into Eqs. (4.2.50)−(4.2.52), the following is obtained:

$$\left(C_1\left(m\pi\right)^2+C_2+p^2\right)\overline{\varphi}_m+\left(C_3\left(m\pi\right)^3+C_4\left(m\pi\right)\right)\overline{\Omega}_m+C_5\left(m\pi\right)\overline{\Phi}_m=0, \tag{4.2.55}$$

$$\left(C_6\left(m\pi\right)^3+C_7\left(m\pi\right)\right)\overline{\varphi}_m+\left(C_8\left(m\pi\right)^4+C_9\left(m\pi\right)^2+p^2\right)\overline{\Omega}_m=F_m, \tag{4.2.56}$$

$$-\left(p^2+\tau_1 p^3\right)\left(m\pi\right)C_{12}\overline{\varphi}_m+\left[\left(p_0+p\right)\left(\left(m\pi\right)^2+C_{10}\right)+\left(p^2+\tau_1 p^3\right)C_{11}\right]\overline{\Phi}_m=0. \tag{4.2.57}$$

Solving Eqs. (4.2.55) – (4.2.57) for $\overline{\Omega}_m\left(p\right)$ gives the following expression:

$$\overline{\Omega}_m\left(p\right)=F_m\frac{a_0+a_1p+a_2p^2+a_3p^3+a_4p^4+a_5p^5}{b_0+b_1p+b_2p^2+b_3p^3+b_4p^4+b_5p^5+b_6p^6+b_7p^7}. \tag{4.2.58}$$

The solution of normalized deflection $\Omega_m\left(\tau\right)$ is obtained after taking Laplace inverse transform of Eq. (4.2.58). The solution yields

$$\Omega_m\left(\tau\right)=F_m\sum_{i=1}^{6}\left(\frac{a_0+a_1\beta_i+a_2\beta_i^2+a_3\beta_i^3+a_4\beta_i^4+a_5\beta_i^5}{b_1+2b_2\beta_i+3b_3\beta_i^2+4b_4\beta_i^3+5b_5\beta_i^4+6b_6\beta_i^5+7b_7\beta_i^6}\right)e^{\left(\beta_i\tau\right)}, \tag{4.2.59}$$

where β_i are the solutions of the equation $b_0+b_1\beta+b_2\beta^2+b_3\beta^3+b_4\beta^4+b_5\beta^5+b_6\beta^6+b_7\beta^7=0$. As a result of the inverse Laplace transform of Eq. (4.2.49), the normalized deflection can be calculated as follows:

$$\begin{aligned}\Omega_m\left(x,\tau\right)&=\sum_{m=1,3,..}^{\infty}\Omega_m\left(\tau\right)\sin(m\pi x)\\&=\sum_{m=1,3,..}^{\infty}\left[F_m\sum_{i=1}^{6}\left(\frac{a_0+a_1\beta_i+a_2\beta_i^2+a_3\beta_i^3+a_4\beta_i^4+a_5\beta_i^5}{b_1+2b_2\beta_i+3b_3\beta_i^2+4b_4\beta_i^3+5b_5\beta_i^4+6b_6\beta_i^5+7b_7\beta_i^6}\right)e^{\left(\beta_i\tau\right)}\right]\sin(m\pi x).\end{aligned} \tag{4.2.60}$$

Furthermore, the normalized thermal moment can be obtained as

$$\Phi_m(x,\tau) = \sum_{m=1,3,..}^{\infty} \Phi_m(\tau)\sin(m\pi x)$$
$$= \sum_{m=1,3,..}^{\infty} \left[F_m \sum_{i=1}^{6} \left(\frac{f_2\beta_i^2 + f_3\beta_i^3}{b_1 + 2b_2\beta_i + 3b_3\beta_i^2 + 4b_4\beta_i^3 + 5b_5\beta_i^4 + 6b_6\beta_i^5 + 7b_7\beta_i^6} \right) e^{(\beta_i\tau)} \right] \sin(m\pi x), \tag{4.2.61}$$

where $f_2 = -C_{12}d_2(m\pi)$, $f_3 = -C_{12}d_2(m\pi)\tau_1$.

4.2.5 Numerical results and discussion

A detailed numerical simulation for a Silicon Timoshenko beam is conducted in this subsection in order to estimate the dimensionless deflection and thermal moment as derived in the previous subsection. At the reference temperature $T_0 = 300K$, the numerical data for Silicon beams is the same as in the previous subchapter 4.1.

The two aspect ratios are considered here, namely length to height of the beam $\left(\frac{L}{h}\right)$, and material length scale to height of beam $\left(\frac{l}{h}\right)$. The ranges of dimensionless relaxation parameter τ_1 and material length scale parameter l are considered as $(1.2 \leq \tau_1 \leq 1.3)$ and $(0 \leq l \leq 0.6)$, respectively. It is assumed that transverse load $f = \frac{EAh}{L^2}$, so $f_0^* = 1$.

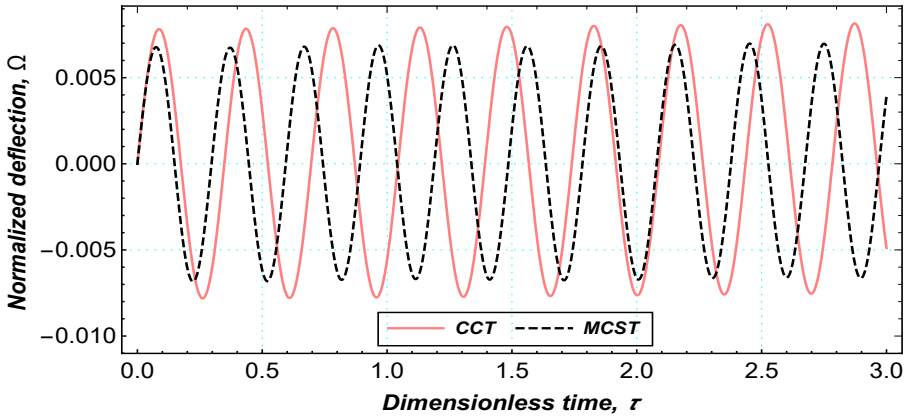

Figure 4.2.2: Size-dependent deflection for CCT and MCST with respect to dimensionless time τ

Under the MGT heat conduction model, a comparison is performed in Fig. 4.2.2

for midspan normalized dynamic deflection for classical ($l = 0$) and the non classical (MCST) theories in the dimensionless time interval $(0 - 3)$. The graph in Fig. 4.2.2 clearly illustrates how the amplitude of dynamic deflection is gradually attenuated under both the theories. This attenuation causes a higher vibration frequency in case of MCST with MGT model as compared to the CCT with MGT model implying that the energy dissipation rate, which causes the attenuation of deflection, is much higher under MCST than CCT for MGT heat conduction model. Moreover, as dimensionless time τ increases, the vibration frequency increases while the amplitude of normalized deflection decreases. In the small period of time, crest value for dimensionless midspan dynamic deflection is essentially identical under two theories. However, a significant difference is observed as time passes. The maximum and minimum amplitudes of deflection varies significantly and the peaks are attained earlier in case of MCST as compared to CCT.

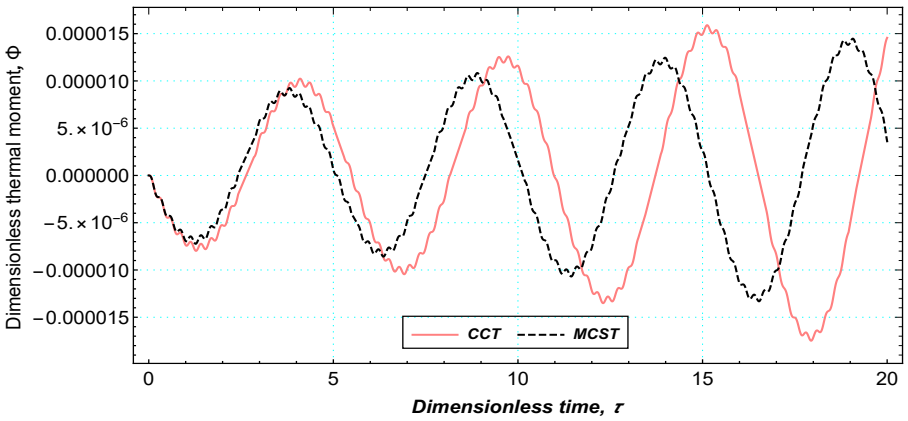

Figure 4.2.3: Variation of thermal moment for CCT and MCST with respect to dimensionless time τ $(L/h = 10)$

Fig. 4.2.3 depicts the midspan dimensionless thermal moment for the dimensionless time period (0–20) to emphasize differences in results under CCT and MCST. The aspect ratio of microbeam length to thickness is considered as $\frac{L}{h} = 10$ for these curves to simulate the thermal moment propagation under MGT heat conduction model. It is important to note here that the phase difference of the midspan thermal moment becomes wider as the dimensionless time τ intensifies. For both the theories, it can

be noticed that as τ increases, the amplitude of thermal moment increases while the frequency of vibration decreases. It is further observed that peak values of thermal moment under MCST is sufficiently less than that predicted by CCT, which is reasonable cause for more energy dissipation inside the microbeam. This becomes more significant as time increases. Fig. 4.2.3 clearly shows that in contrast to the dynamic deflection behavior, the thermal moment's peak points arise at greater values as time increases.

Figs. 4.2.4(a,b) plot the behavior of midspan normalized deflection for different aspect ratios with microbeam length to thickness $\frac{L}{h}$=30, 60, and 90. Here, the occurrence of steady state form of dimensionless deflection is separately illustrated for the cases when material parameter $l = 0.3$ and 0.6. Contrasting effect of aspect ratio $\frac{L}{h}$ and material length parameter l on normalized deflection is clearly visible. In terms of aspect ratio, it is noticeable that as $\frac{L}{h}$ intensifies, the steady state amplitude of deflection attains its peak value while occurrence of oscillation diminishes. From these plots, one can observe that energy dissipation rate is higher for larger values of material length parameter l. Hence, the oscillation under lower material length parameter l will occur for longer period as compared to oscillation under higher value of parameter l.

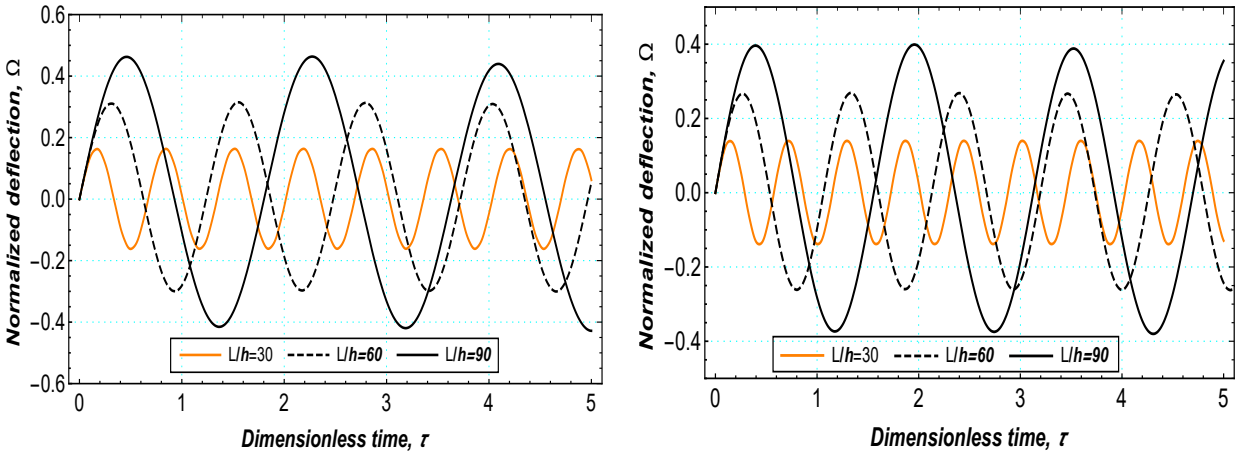

Figure 4.2.4: (a) Size-dependent deflection for different aspect ratio L/h when l =0.3. (b) Size-dependent deflection for different aspect ratio L/h when l =0.6.

For MCST theory, the effect of aspect ratio (microbeam length to thickness) in midspan thermal moment against dimensionless time τ is highlighted in Figs. 4.2.5(a,b). Here, we consider several values of , $\frac{L}{h}$ $\left(\frac{L}{h} = 12, 14 \text{ and } 16\right)$. The effects of aspect ratio in simulation of thermal moment propagation for initial range of dimensionless time interval is barely noticeable. However, as time progresses, the elevation in the peaks of thermal moment propagation becomes more prominent inside the microbeam indicating a significant effect of aspect ratio on thermal moment. The phase discrepancy between the transient outputs of the thermal moment occurs owing to a variation in aspect ratio, like the dynamic deflection performance. It can be seen that the impact of thermal moment gradually reduces with an increase in the value of material parameter l.

The effect of length scale parameter ratio $\frac{l}{h}$, $\left(\frac{l}{h} = 0,\ 0.2, 0.4 \text{ and } 0.6\right)$ to microbeam thickness in the dimensionless midspan deflection is depicted in the Fig. 4.2.6 which presents the results for CCT and MCST to highlight the normalized deflection against to dimensionless time τ. The amplitude of deflection under classical couple stress theory $\left(\frac{l}{h} = 0\right)$ arrives maximum as compared to MCST. According to classical theory, due to the less frequency of vibration, the rate of attenuation in normalized deflection is substantially slower than MCST. It is also worth noting that increase in the ratio (l/h) increases the phase difference drastically. Moreover, the peak values of normalized deflection is obtained at smaller time with the increase in aspect ratio $\frac{l}{h}$.

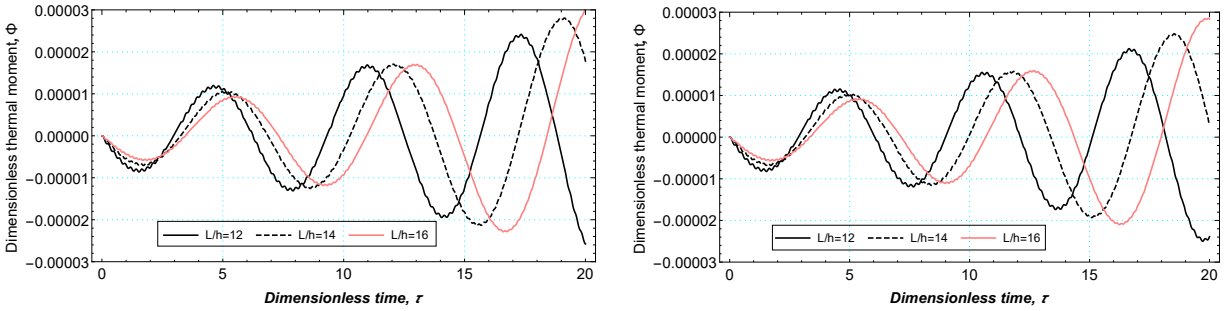

Figure 4.2.5: Variation of thermal moment for different aspect ratio (L/h) with length to height (a) when l=0.3 (b) when l=0.6.

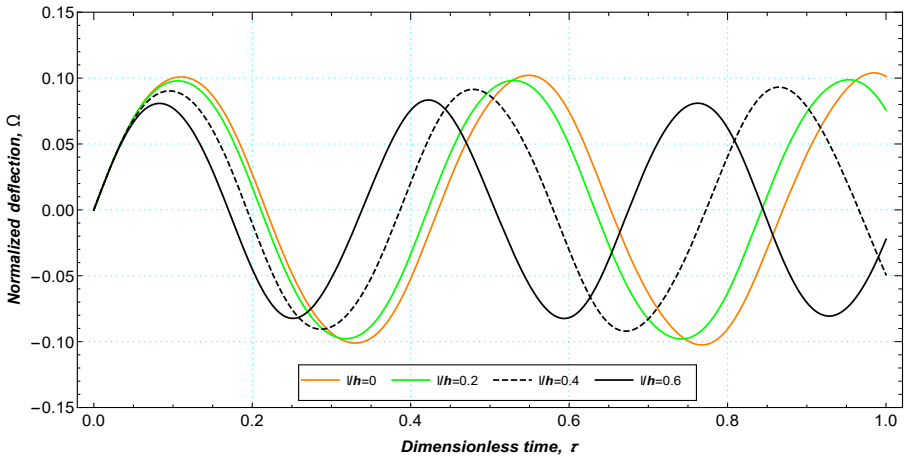

Figure 4.2.6: Size-dependent deflection for ratios with material length scale parameter to thickness (l/h) along dimensionless time τ

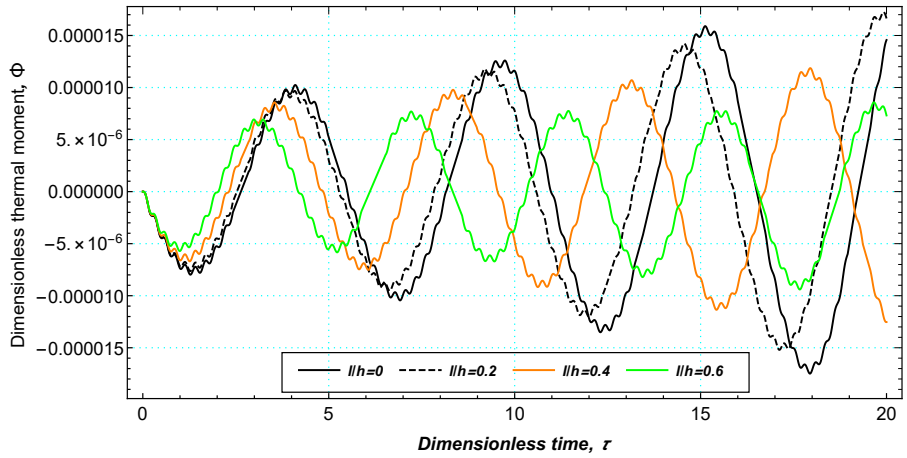

Figure 4.2.7: Thermal moment propagation for ratios with material length scale parameter to thickness (l/h) along dimensionless time τ

The propagation of dimensionless thermal moment for length scale parameter ratio $\frac{l}{h}$, $\left(\frac{l}{h} = 0,\ 0.2, 0.4 \text{ and } 0.6\right)$ against dimensionless time τ is demonstrated in Fig. 4.2.7 The CCT and MCST have been considered to illustrate the size effect. The significant diminution in thermal moment propagation is visible for a higher aspect ratio. This means that by using CCT, the thermal moment response becomes greater than the extracted thermal moment propagation under MCST.

The variation of thermal moment versus time for different reference temperature T_0,

$(293K, 400K, \text{and } 500K)$ is plotted in Fig. 4.2.8. The outcomes of these plots are shown under assumption of aspect ratio $\frac{L}{h} = 0.5$. The responses of the thermal moment under different reference temperature is prominent. As the temperature intensifies, the change in thermal moment is quite significant. It is observed that the domain of thermal moment increases as reference temperature goes to a higher range.

In order to illustrate the behavior of three generalized thermoelastic theories (LS, GN-III and MGT), the midspan deflection is plotted as a function of the time in Fig. 4.2.9. In this numerical simulation, the aspect ratio is fixed as $\frac{L}{h} = 0.3$ in the context of MCST. It is observed that amplitude of deflection via all three models exactly match with each other. It means that all three generalized thermoleastic theories provide steady state deflection in this time range. Therefore, the frequency of vibration does not alter measurably as a result of incorporating relaxation time into the model. This graph shows that these theories have negligible diminution in amplitude of normalized deflection. However, Fig. 4.2.10 demonstrates that the thermal moment's response for the MGT is significantly different from the response under the GN-III model, although the responses under MGT and LS models are identical. Higher amplitudes of thermal moment are observed in case of MGT model as compared to the GN-III model.

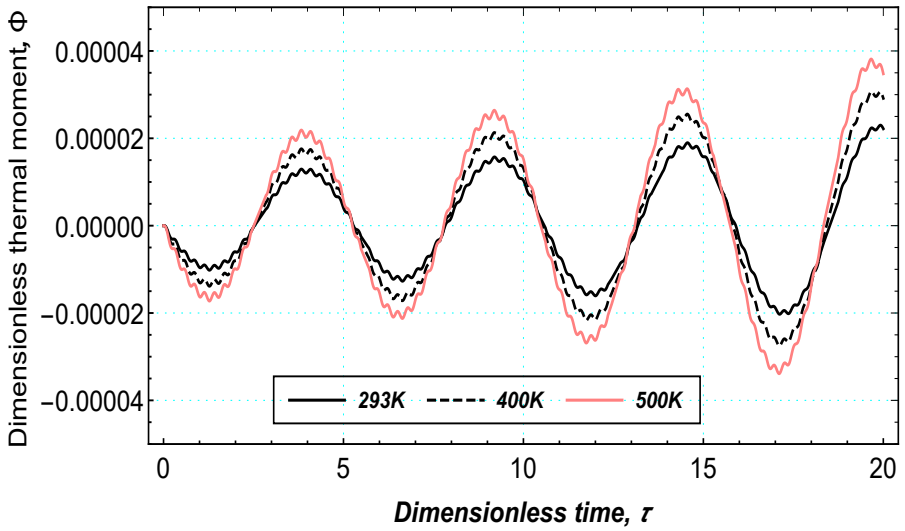

Figure 4.2.8: Thermal moment variation for different reference temperature T_0 with respect to dimensionless time τ

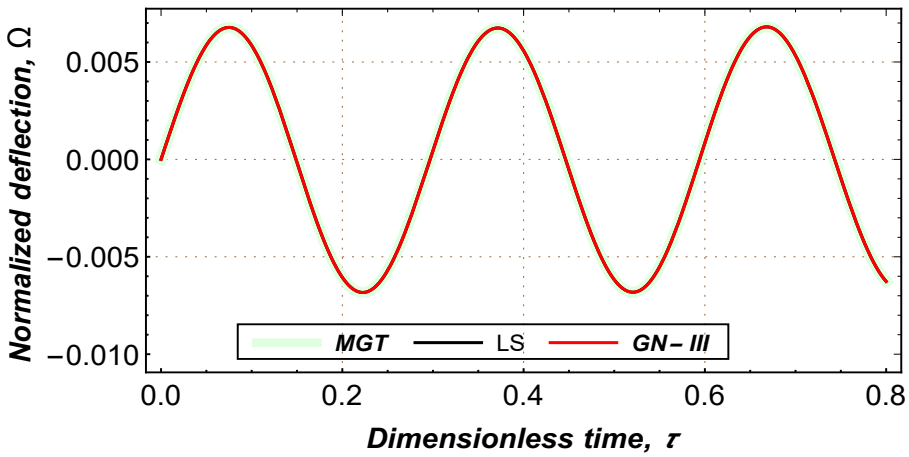

Figure 4.2.9: Size-dependent deflection for different generalized thermoelasticity theories (LS, GN-III and MGT) with respect to dimensionless time τ.

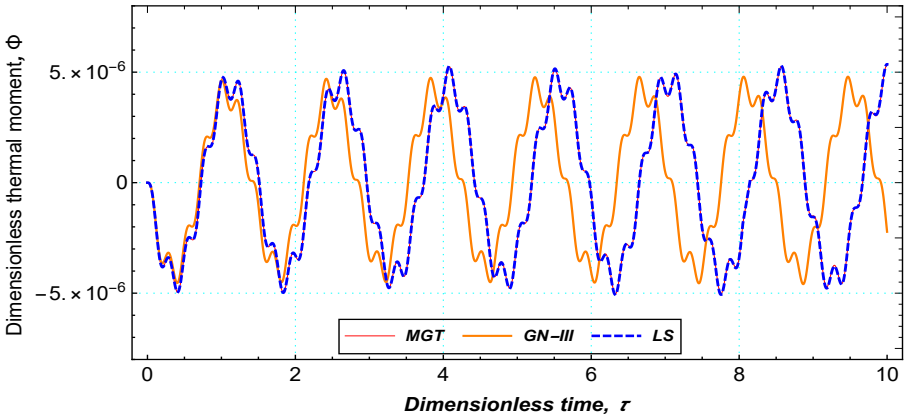

Figure 4.2.10: Thermal moment variation for different generalized thermoelasticity theories (LS, GN-III and MGT) with respect to dimensionless time τ.

4.2.6 Conclusion

This current work investigates behavior of deflection and the propagation of thermal moment of the simply supported Timoshenko beam in the context of MGT heat conduction model. In order to capture the dynamic behavior of Timoshenko beam, the CCT and non-classical (MCST) theories are considered into present work. The normalize coupled thermoelastic equations and boundary conditions are obtained by employing the Hamilton's principal (variational approach). Under the MGT model, findings are

compared to those acquired by the MCST and CCT. Several features of the theories are highlighted in previous section. The following are some key conclusions of this work:

- MCST under MGT heat conduction has a significantly higher energy dissipation rate due to deflection attenuation than the CCT theory.
- The elevation in the peak values of thermal moment gets more noticeable as time goes on. The peak values of thermal moment increase progressively as time intensifies.
- The effects of aspect ratios $\left(\frac{L}{h}\text{ and }\frac{l}{h}\right)$ on deflection and thermal moment propagation are prominent. If the aspect ratio increases in proportion to the length scale parameter l, there is a faster frequency response, resulting in increased energy dissipation.
- As the reference temperature rises, the thermal moment's propagation range also rises.
- There is no significant difference between the vibration characteristics of the deflection for the MGT, LS, and GN-III models.
- MGT and LS models display a wider range of thermal moment, while the GN-III model displays a smaller range of thermal moment. The MGT model predicts more similar behavior with LS theory.